

Conformational change and protein–protein interactions of the fusion protein of Semliki Forest virus

Don L. Gibbons^{1,2}, Marie-Christine Vaney¹, Alain Roussel^{1*}, Armelle Vigouroux¹, Brigid Reilly², Jean Lepault¹, Margaret Kielian² & Félix A. Rey¹

¹Virologie Moléculaire & Structurale, UMR 2472/1157 CNRS-INRA, 1 Avenue de la Terrasse, 91198 Gif-sur-Yvette Cedex, France

²Department of Cell Biology, Albert Einstein College of Medicine, 1300 Morris Park Avenue, Bronx, New York 10461, USA

* Present address: AFMB, CNRS UMR 6098, 31 Chemin Joseph Aiguier, 13402 Marseilles, France

Fusion of biological membranes is mediated by specific lipid-interacting proteins that induce the formation and expansion of an initial fusion pore. Here we report the crystal structure of the ectodomain of the Semliki Forest virus fusion glycoprotein E1 in its low-pH-induced trimeric form. E1 adopts a folded-back conformation that, in the final post-fusion form of the full-length protein, would bring the fusion peptide loop and the transmembrane anchor to the same end of a stable protein rod. The observed conformation of the fusion peptide loop is compatible with interactions only with the outer leaflet of the lipid bilayer. Crystal contacts between fusion peptide loops of adjacent E1 trimers, together with electron microscopy observations, suggest that in an early step of membrane fusion, an intermediate assembly of five trimers creates two opposing nipple-like deformations in the viral and target membranes, leading to formation of the fusion pore.

Membrane rearrangements take place throughout the lifespan of a cell and are essential to all forms of life¹. Stable membranes do not fuse spontaneously, and specific fusion proteins tightly control all membrane fusion events through interactions with lipids and with other fusion proteins. Much of our knowledge of membrane fusion has come from the study of viral membrane proteins that interact with lipids to induce fusion during viral entry. The best-studied example of a membrane fusion protein is the influenza virus haemagglutinin, a prototypic class I fusion protein². Although many features of the molecular mechanisms of membrane fusion are not understood, the class I studies suggest a model in which fusion is driven by the formation of a stable protein rod anchored in both the target and donor membranes³. Several such hairpin-like structures could act cooperatively^{4–6} to induce the formation of a fusion pore connecting the two membrane-bound compartments^{7,8}, although the mechanisms by which such synergistic interactions might drive fusion are not clear.

Semliki Forest virus (SFV), a member of the alphavirus genus, has been used as a model system to define virus endocytic entry⁹. Alphaviruses have two type I glycoproteins anchored at their surface, E1 (membrane fusion protein) and E2 (receptor binding protein), organized with a T = 4 icosahedral architecture¹⁰. The crystal structure of the neutral-pH form of the E1 ectodomain has been determined¹¹ and fitted into medium-resolution (9 Å) cryo-electron microscopy (EM) reconstructions of SFV¹¹ and Sindbis virus particles¹². These studies have shown that E1 lies in a tangential orientation at the viral surface, forming an icosahedral scaffold covering the viral membrane, whereas E2 forms projecting spikes at the three-fold and quasi-three-fold axes of the T = 4 icosahedral lattice of the viral surface. In this arrangement, E2 prevents E1–E1 contacts about three-fold axes of the particle. The crystal structure of E1 revealed an unanticipated homology with the envelope protein E of flaviviruses^{13,14}, with identical topology and a very similar three-domain arrangement of the polypeptide chain. These ‘class II’ membrane fusion proteins¹¹ are folded mostly as β-sheets, with the internal fusion peptide (referred to here as the ‘fusion loop’ or ‘cd loop’) in a loop between two β-strands. During virus entry, the acidic environment of the endosome triggers an

irreversible conformational change in E1, from an E1/E2 heterodimer at the viral surface to a target-membrane-inserted E1 homotrimer¹⁵. This rearrangement of E1 leads to fusion of the viral and endosomal membranes, releasing the virus genomic RNA into the cytoplasm of the cell¹⁶.

The E1 ectodomain has been shown to behave similarly to its full-length, virus-anchored counterpart^{17,18}. This fragment, termed E1* and lacking amino acids 392–438 at the carboxy terminus of the protein, changes from a soluble monomer to a trimer as it inserts into liposomes upon exposure to low pH¹⁷. E1* membrane insertion exhibits the same lipid dependence as alphavirus fusion, requiring both cholesterol and sphingolipid in the target membrane¹⁹. Electron micrographs of liposomes containing E1 or E1* inserted through low-pH treatment showed that both proteins reorient vertically with respect to the membrane to produce trimers of very similar shape and dimensions²⁰. Although the depth of membrane insertion was not certain, the images suggested a possible lipid-bilayer-spanning topology for domain II (see Fig. 1 for the definition of protein domains), with the fusion loop and the transmembrane (TM) anchor at the same side of a stable protein rod, similar to the hairpin structure of post-fusion class I proteins.

Here, we have solubilized the E1* trimer from liposomes, crystallized it in the presence of detergents and determined its three-dimensional (3D) structure to 3.3 Å resolution. This structure shows that the low-pH-triggered trimeric form of E1* has the C-terminal ‘stem’ region, which connects to the TM anchor, directed towards the fusion loop. This observation therefore confirms that a folded-back conformation is a common fusion mechanism for both class I and class II proteins. However, in contrast to the class I proteins²¹, the three domains of E1 maintain their original folds during this conformational change. The E1* fusion loop has an extended conformation, consistent with insertion into only the outer leaflet of the target membrane. The contacts observed in the crystals, along with the symmetry of the rosette-like structures observed by EM, suggest that fusion involves an assembly of several E1 trimers interacting through their fusion loops around the fusion site. These lateral interactions between fusion peptide loops from

adjacent trimers are postulated to have an essential and concerted role in the fusion process.

Tertiary rearrangement of the E1 ectodomain

Figure 1 shows the observed conformational rearrangement of the E1* polypeptide chain induced by low-pH treatment in the presence

of liposomes. There is essentially no change in secondary structure. By contrast, the interactions between the domains constituting the E1 subunit are markedly different. The most important rearrangement concerns domain III, which moves by 37 Å towards the fusion loop. The different location and orientation of domain III redirects the polypeptide chain so that in the trimeric form its C terminus

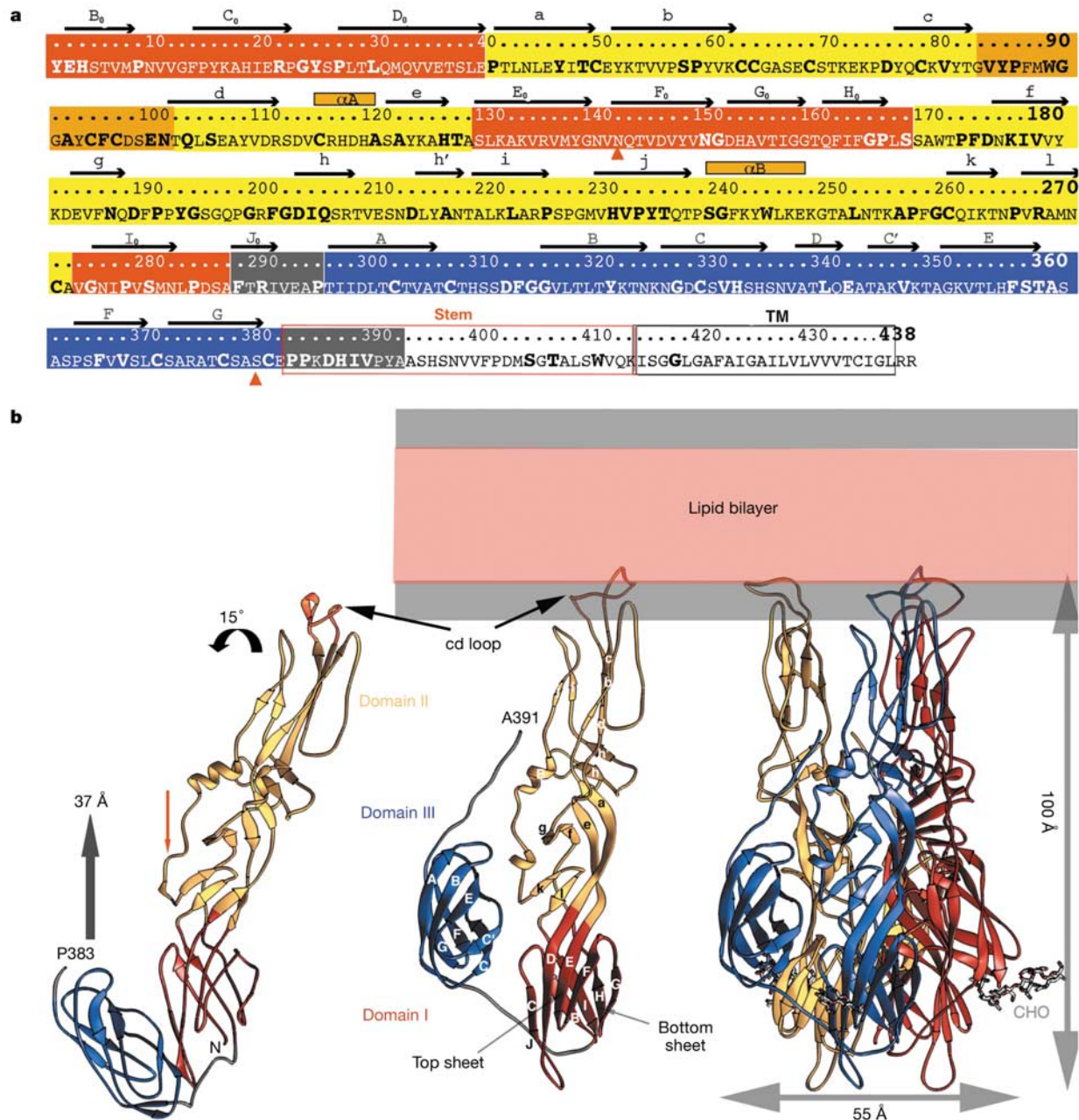


Figure 1 Overall fold of glycoprotein E1. **a**, Amino-acid sequence of SFV E1. Highly conserved residues are highlighted as bold letters in bigger font. Red, yellow and blue backgrounds denote residues belonging to domains I, II and III, respectively. The fusion loop is against an orange background, and the stem and the linker between domains I and III are in grey. The stem and transmembrane anchor are boxed in red and black, respectively. A white background denotes residues absent from the crystallized fragment. Elements of secondary structure (labelled as in ref. 13) are indicated above the sequence. Red triangles underneath the sequence indicate glycosylation sites: *N*-linked at position 141 and *O*-linked at position 379. **b**, Left panel, ribbon diagram of the E1 ectodomain at neutral pH. Thick arrows indicate the major rearrangements. A thin red arrow points to a region of contact described in the text. The N and C termini of the fragment are indicated

by N and P383 (last ordered residue), respectively. Middle panel, the E1* subunit after the conformational change, with elements of the secondary structure labelled. The two forms (left and middle panel) were superposed on the B₀L₀H₀G₀ β-sheet (labelled 'bottom sheet') in domain I. A391 indicates the C terminus of the fragment. A new β-strand, J₀, runs antiparallel to β-strand C₀ in domain I. A sketch of the lipid bilayer, at roughly the same scale as the protein, is indicated at the top, where grey and pink regions indicate lipid heads and lipid aliphatic chain regions, respectively. Right panel, the E1* trimer. Each subunit is coloured differently, with the subunit in blue oriented as in the middle panel. The molecular dimensions are indicated. The *N*-linked carbohydrate is displayed as grey balls and sticks, labelled CHO.

points towards the fusion loop region. A segment of about nine amino acids of the stem (at the extreme C terminus of the E1* fragment), which was not ordered in the crystals of the monomeric neutral-pH form, becomes ordered in the trimer. The E1* fragment ends at residue 391, which lies about 25 Å from the fusion peptide loop. The remaining residues connecting to the TM anchor, 392–413, can easily cover the distance to the lipid bilayer, indicated by the location of the fusion loop. In the trimer, the immunoglobulin-like domain III interacts through its AB loop and strand C' (see Fig. 1 for nomenclature) with amino acids 250–260 of domain II, which lie in a region of relatively extended conformation in the monomeric neutral-pH form (indicated by a red arrow in Fig. 1b, left panel). The contact induces a slight winding of this domain II segment, which packs against strand g and the kl hairpin. A consequence of this interdomain interaction is to pull down helix α B, bringing with it the tip of domain II, which rotates by 15° about a hinge located between β -sheets kD₀E₀ and gfeah (indicated in Fig. 1b), resulting in a straight continuous rod containing domains I and II. This interaction is stabilized by the fragment of the stem present in the structure (grey in Fig. 1).

The fusion cd loop (orange in Fig. 1) displays a higher average temperature factor than the rest of the molecule. It unwinds with respect to the neutral-pH soluble form, displaying a rather extended conformation that is not compatible with penetration of the aliphatic moiety of the membrane. It exposes several aromatic side chains that are very probably interacting with disordered

detergent molecules in the crystal. Assuming that the observed conformation of the fusion loop does indeed correspond to its membrane-interacting conformation, our data suggest that the glycine-rich main chain interacts tightly with the lipid heads, projecting aromatic side chains into the aliphatic region of the lipid bilayer. This loop shows considerable plasticity, adapting to the particular contact in the crystal, as discussed below.

Overall architecture of the E1* trimer

The subunits associate in a parallel arrangement in the trimer, such that the fusion loops are at the same side of a stable elongated molecule, as shown in Fig. 1b. Each subunit in the E1* trimer buries an area of 4,300 Å² from solvent accessibility. The extent of the contacts is reflected in the observed stability of the molecule^{18,22}. The trimer is formed essentially by the central interactions of the bottom β -sheet of domain I (formed by strands G₀H₀I₀B₀, see Fig. 1) and is continued in domain II by contacts between elements at its domain I proximal half. The latter involve, on one side, residues spanning helix α B all the way to the beginning of β -strand k and, on the other, β -sheet gfeah. Domain III packs at the periphery, at the interface between two subunits. The highly conserved residues in alpha-viruses cluster at the fusion loop, at the stem and at the trimer contact regions. Both the trimer surface and the intra-trimer contact areas are essentially hydrophilic. The tips of domain II do not display trimer contacts, and exhibit high temperature factors. The location of the C terminus of the ectodomain suggests that in the final, post-fusion conformation of the full-length trimer, the remaining amino acids of the stem are likely to provide a contact surface to stabilize this region.

Lateral interactions of E1 trimers on membranes

Before the determination of the crystal structure, we derived a model for the E1* trimer from EM data²⁰. This model was based on

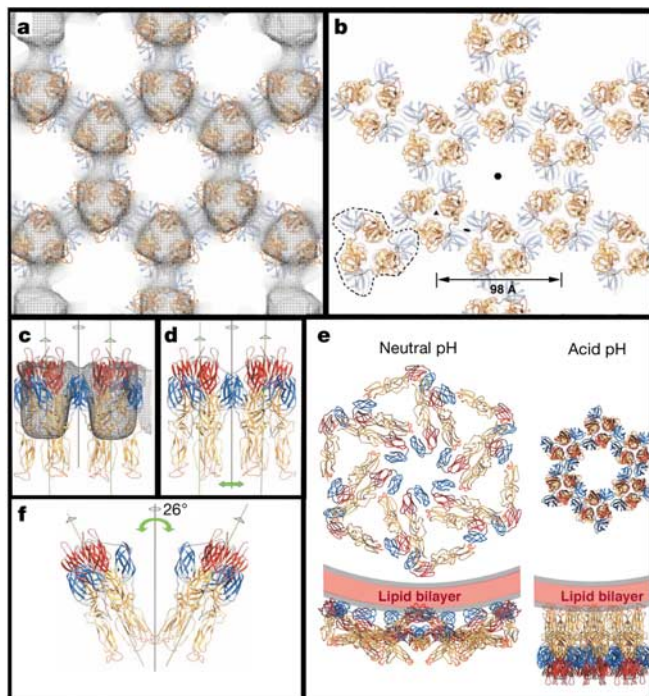


Figure 2 Trimer-trimer interactions observed in the 2D lattice and in the 3D crystals. **a–d**, E1* trimers on the 2D lattice²⁰. **a** and **b** show views from the membrane, **c** and **d** show side views. In **b** and **d**, the reconstruction was removed to visualize the contacts. In **b**, a trimer is outlined with a black broken line. The $\rho 6$ hexagonal cell parameter is indicated (98 Å) and one of each symmetry element (six-fold, three-fold and two-fold axis) is marked with a filled black symbol: hexagon, triangle and ellipse, respectively. In **c** and **d**, the symmetry axes are shown as vertical lines with open symbols. In **d**, a green double arrow indicates that the fusion loops are too far apart to make contacts. **e**, Conformational rearrangement of the virus surface. Left panel, arrangement of E1 at the viral surface at neutral pH^{11,12} (glycoprotein E2 is not shown). Right panel, arrangement of E1* after the conformational change, as observed at the surface of liposomes. First row, top view; second row, side view. **f**, Two-fold contact on the 3D crystal, involving fusion loops. The angle between trimers and dyad is 26°.

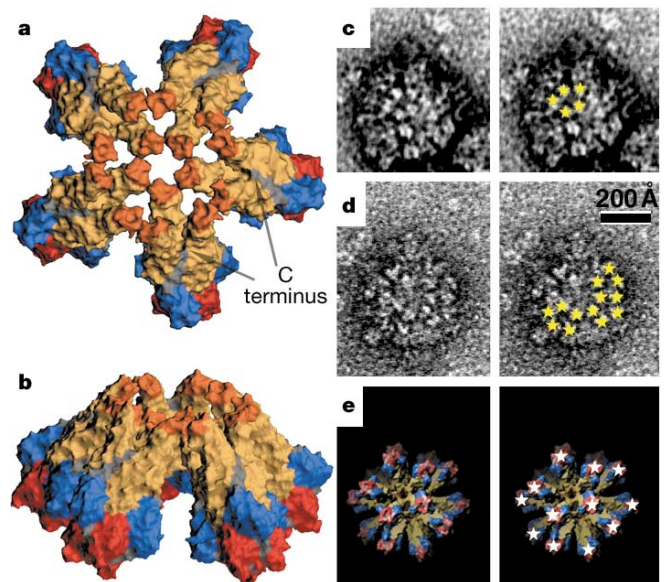


Figure 3 A ring of five trimers of E1*. **a**, **b**, Surface representation of the ring, coloured according to domains, view down the five-fold axis (**a**) and a side view (**b**) slightly tilted to show the depth of the crater. Note the grey stem segment leading to the C terminus of the fragment, indicated by arrows. **c**, **d**, Micrographs of negatively stained rosettes of E1* trimers obtained by dialysing away the detergent used for solubilization. In the right-hand panel, a star was added to highlight the trimers present in rings of five. The three-fold symmetry of some of the trimers is evident, especially on panel **c**. **e**, Model for a symmetric rosette exhibiting dodecahedral symmetry, built according to Supplementary Information. The magnification is about three times that of the rosettes presented in panels **c** and **d**.

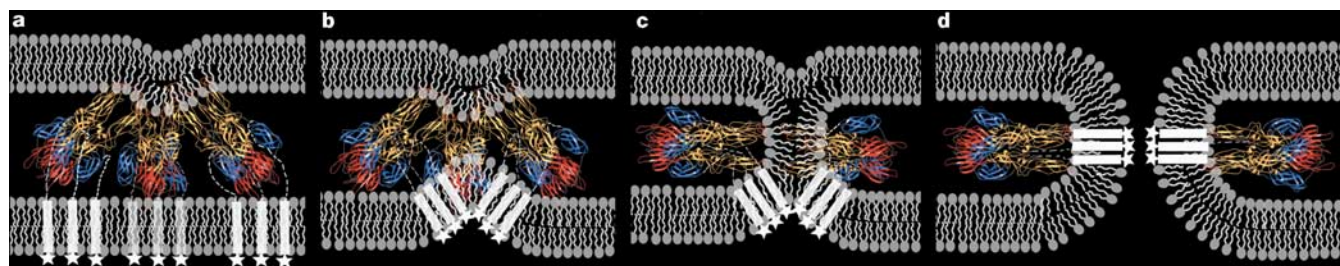


Figure 4 Model for membrane fusion involving protein–protein interactions, as explained in the text. **a–d**, White stars denote hydrophilic residues and C-terminal charge in the cytosolic tail of the fusion protein. White cylinders denote transmembrane anchors.

Broken white lines indicate the stem region, which connects the ectodomain to the TM segments. For clarity, the complete ring of five trimers is not shown.

fitting three E1* subunits, in their neutral-pH form, into a 3D reconstruction calculated from images of negatively stained two-dimensional (2D) arrays of E1*. Because of the low resolution of that reconstruction, we made no attempt at the time to alter the relative orientations of domains within the subunits. The resulting trimer model predicted the observed parallel arrangement of the subunits, but was longer than the actual structure of the E1* trimer because the rearrangement of domain III was not taken into account. Indeed, on the basis of cryo-EM observations of E1*-containing liposomes, we had speculated that domain II might actually cross the lipid bilayer. The predicted length of the trimer was roughly consistent with the height of the extramembrane domain plus a membrane-inserted domain of approximately the thickness of the lipid bilayer. Here we revise the model for E1* membrane insertion by taking into account the fact that the observed conformation of domain II in the crystal structure is incompatible with a membrane-spanning topology, and that the total length of the molecule is shorter because domain III is displaced towards the fusion loop. To better understand the interactions of E1* trimers in the 2D arrays, we have now fitted the experimentally determined structure of the E1* trimer into the previous 3D reconstruction, as described in Methods. As shown in Fig. 2, the trimers make lateral contacts through dyads of the *p6* lattice. The side view (Fig. 2c) shows that the EM reconstruction imaged only the thicker portion of the molecule. The three legs of the ‘tripod’ (that is, the tip of domain II) were not visualized, presumably owing to the reduced mass and increased flexibility caused by the absence of subunit contacts within this portion of the trimer. The trimers display a parallel arrangement in the 2D lattice, with the heads touching but with the ‘legs’ too far apart to make inter-trimer contacts. However, the extensive contacts between fusion loops from adjacent trimers observed in both the 3D crystals and the trimer rosettes (as explained in the following paragraphs) suggest that the fusion loop interaction is likely to be maintained in the hexagonal 2D lattice. Such fusion loop contacts would force the

playing of the domain II legs, allowing the trimer to make contacts through both the head and fusion peptide loops in the 2D lattice. It is noteworthy that the full-length E1 trimer does not form regular lattices on membranes, suggesting that the presence of the stem region stabilizes the legs and prevents the parallel trimer arrangement in a hexagonal lattice (see Supplementary Information).

Figure 2e compares the interactions of E1* trimers in the hexagonal lattice with the interactions of the neutral-pH E1 on the virus surface. In both panels (neutral and acid pH) the same number of E1* subunits is displayed (18 subunits). The surface covered by E1 in the neutral-pH form is more than three times larger than that covered by its low-pH-induced trimeric form. During infection, it is likely that only the E1 molecules most proximal to the endosome membrane can actually interact with it. Rearrangement of the remaining E1 molecules in the virus particle may have a further role in destabilizing the virion membrane to facilitate the membrane fusion process.

Inter-trimer contacts through fusion loops

Insertion of E1 into target membranes seems to be a cooperative process, and depends critically on the lipid composition of the target membrane^{19,20}. Furthermore, the membrane fusion reaction triggered by viral fusion proteins in general is thought to involve interactions between several trimers^{4,5}, which may interact through the fusion loops at the same time as they interact with membranes. In this first structure of a membrane fusion protein containing the membrane-interacting form of the fusion peptide, it is important to examine the possible types of contact between trimers that are mediated by the fusion loop. Figure 2f shows the main contact between trimers in the crystal, termed contact 1 in Supplementary Information. This contact is made across a two-fold axis, but with the trimer axis tilted 26° with respect to the dyad, instead of being parallel as in the 2D lattice. The same surface of the trimer faces the dyad in both the 3D and the 2D crystals, as deduced from the fitting to the EM density. Contact 1 takes place exclusively through the

Table 1 Phasing statistics as a function of resolution*

Resolution range	Completeness (%)	Signal-to-noise ratio	Isomorphous phasing power (centric reflections)†	Isomorphous phasing power (acentric reflections)†	Anomalous phasing power‡	Overall figure of merit (acentric)‡	Overall figure of merit (centric)‡
50.14–8.91	99.9	28.03	0.99	1.34	2.28	0.85	0.55
8.91–6.35	99.9	25.00	1.08	1.56	2.90	0.82	0.52
6.35–5.20	99.8	23.91	1.09	1.48	2.82	0.76	0.48
5.20–4.51	99.4	23.45	0.77	1.14	2.14	0.72	0.44
4.51–4.04	99.4	17.81	0.73	0.92	1.61	0.62	0.41
4.04–3.69	99.0	11.97	0.60	0.64	0.99	0.45	0.26
3.69–3.42	98.9	10.56	0.45	0.48	0.77	0.34	0.18
3.42–3.20	71.9	8.49	0.57	0.49	0.83	0.22	0.15
Overall	96.0	15.17	0.91	1.07	1.81	0.54	0.38

Refinement statistics: resolution range, 20–3.2 Å; number of reflections, 40,912; working set, 38,837 reflections; *R* factor, 0.265; free set, 2,075 reflections; free *R* factor, 0.285. r.m.s.d. bonds, 0.010006 Å; r.m.s.d. angles, 1.6°. r.m.s.d. domain superposition of neutral/acid-pH forms: domain I, 2.43 Å; domain II, 1.76 Å; domain III, 1.0 Å.

*Statistics calculated using the program SHARP²⁷.

†The phasing power statistics corresponds to each crystal separately. We took a representative crystal to fill these columns.

‡The reported figure of merit corresponds to the phases before any density modification.

glycine-rich, flexible fusion peptide loops. These interactions are therefore likely to adapt to different geometries and, in particular, to different angles between trimers.

If, in contrast to the 3D crystals, where the packing environment of the trimers is not three-fold symmetric, three-fold symmetry is imposed on the two trimers involved in contact 1, it is possible to create a closed arrangement of trimers, the symmetry of which depends on the angle between the trimer axis and the dyad as explained in Supplementary Information. A ring of five trimers making identical interactions best matches the experimentally observed packing angle in the crystal. Figure 3a, b shows such a ring, generated by changing the angle observed in the crystal from 26° to 21°, which is the angle between triads and dyads surrounding the five-fold axes of a dodecahedron. EM observations of E1* rosettes, obtained when the detergent is removed from purified, detergent-solubilized E1* trimers, did indeed reveal the presence of rings of five trimers (Fig. 3c–d). The rosettes are irregular, in keeping with the alternative possible arrangements of three, four or six trimers described in Supplementary Information, but they show the presence of several five-trimer rings. For comparison, Fig. 3e shows a rosette generated from the crystal structure by introducing three identical fusion loop contacts into each of the 20 trimers present in a dodecahedron, with the fusion loops buried in the interior. During the interactions of the trimer with membranes, however, the geometry of the lipid bilayer is likely to restrict the assembly and allow only the formation of one pentagonal face of the dodecahedron, as the other faces would be out of the plane of the membrane.

An intermediate assembly in fusion

The interactions observed between fusion loops, together with the five-trimer rings visualized by EM, suggest that the E1* trimer may correspond to the three-fold symmetric portion of an intermediate made by the full-length E1 molecule while anchored simultaneously to the target and viral membranes. In such an intermediate, the remaining C-terminal stem region, absent in E1*, is likely to be an adaptor in a transient break of three-fold symmetry occurring during the fusion process, whereas the final fully symmetric molecule would have both the stem and TM domains in place. In such a model, the role of this stem segment would be to bring the viral membrane anchor into place in the final fully symmetric molecule. Following insertion of the fusion peptide into the target membrane, this final conformation can only be reached by the trimer within a fused membrane. These E1 conformations together suggest a model for the concerted actions of E1 during fusion, as illustrated in Fig. 4. The ring of five trimers displayed in Fig. 3a, b has a volcano appearance, with a crater formed by five fusion loops at the base and ten at the rim. If each fusion loop is postulated to interact with the lipid heads of the membrane, both at the rim and at the base of the crater, a nipple-like deformation of the target lipid bilayer will be induced, as indicated in Fig. 4a. In this first intermediate, the TM anchors are attached to the viral membrane and the stem has not yet found its expected location in the final post-fusion form of E1. This arrangement will pull the TM segments towards the fusion loop, introducing a second nipple in the viral membrane, exactly under the one formed in the target membrane (Fig. 4b). The stem is expected to interact tightly with the body of the E1* trimer in the final, post-fusion form of the full-length E1 molecule. In this process, the stem will also induce the opposite curvature on the viral membrane while forcing it against the nipple formed in the target membrane, effectively forcing the outer leaflets of the two membranes to merge and form a hemifusion stalk (indicated in Fig. 4c). The presence of hydrophilic residues at the cytoplasmic side, or even just the negative charge of the C terminus of the polypeptide chain (indicated by stars) would prevent the TM segments from entering the stalk. Completion of the conformational change of the protein to reach its final, lowest-energy form, in

which the trimer is fully three-fold symmetric, can therefore be achieved only by forcing formation of a pore (Fig. 4d). The proposed initial aqueous pore would thus be lined by the cytosolic C-terminal end of the fusion protein. This model is in agreement with observations on the human immunodeficiency virus, in which the formation of the six-helix bundle of gp41 was completed only immediately after pore formation²³. It also explains why substitution of the TM anchor in influenza haemagglutinin by a glycosyl phosphatidylinositol (GPI) anchor²⁴, or truncation of the anchor so that it can no longer cross the viral membrane²⁵, leads only to hemifusion. Similar results were reported for C-terminal truncations of the paramyxovirus SV5 fusion protein²⁶. The proposed model may also help to explain in part the observed effect of the cytoplasmic tail of several retroviruses in controlling fusion^{27,28}. The intermediate depicted in Fig. 4c very likely corresponds to the 'restricted hemifusion' state observed in the case of influenza²⁹ and rabies virus³⁰. In such a state, in spite of continuity between the two outer leaflets, the lipids cannot freely diffuse past the ring formed by the TM segments of the fusion protein, resulting in the observed effect. Transition from the step shown in Fig. 4c to that shown in Fig. 4d is likely to involve overcoming a high energy barrier. It has indeed been observed in the case of influenza haemagglutinin that reaching the fusion pore state from the restricted hemifusion state is strongly temperature dependent³¹.

Concluding remarks

Our data, obtained using the independent approaches of X-ray crystallography and EM, provide the first structural evidence for protein–protein interactions between fusion proteins, postulated as essential for membrane fusion. In addition, the results presented in this and in the accompanying manuscript on the dengue virus glycoprotein³², as well as the structure of the tick-borne encephalitis flavivirus envelope protein in its low-pH-induced trimeric form³³, provide a clear link between the class I and class II viral fusion proteins. The analogies in the folded-back conformations and the ability of the SFV membrane fusion model to explain the intermediates observed with class I fusion proteins strongly suggest that both classes act by a single, universal mechanism to cause membrane fusion. □

Methods

Structure determination

The detailed protein preparation and crystallization procedures are described separately³⁴. Briefly, E1*-containing liposomes were prepared as in ref. 20 and were solubilized with *n*-octyl glucoside. The lipids were removed by extensive washing through a vivaspin microfilter, 100 kDa cutoff. For crystallization trials, the detergent was exchanged while concentrating using the same vivaspin microconcentrators. The best crystals grew at 4 °C in the presence of 15 mM of the detergent DDAO (*N,N*-dimethyl decylamine-*N*-oxide), 250 mM NaBr, 25 mM Tris-HCl and 2.5–12.5% PEG 400, pH 4. They belong to the trigonal space group *P*3₁21 with cell parameters *a* = *b* = 198 Å and *c* = 116 Å. For data collection, the crystals were transferred to a cryoprotectant solution containing 30% PEG 400 and 25% glycerol, mounted into cryo-loops and flash-cooled by plunging into liquid ethane. Native crystals diffracted to about 3.7 Å, but heavy-atom soaks with 10 mM HoCl₃ yielded diffraction to 3.1 Å. The best diffracting crystals were subsequently grown in the presence of 10 mM HoCl₃. The structure was solved by a combination of MAD/isomorphous replacement methods using Ho³⁺ as heavy-atom derivative and anomalous scatterer.

The crystals diffracted to about 3.1 Å along *c** and to 3.3 Å along *a**, but were very radiation sensitive and decayed so that the diffraction pattern reached only about 3.9 Å after five to ten images at 100°K. Diffraction data from 15 crystals (all grown in the presence of Ho³⁺) were therefore combined to obtain a complete and redundant data set (at three wavelengths around the Ho³⁺ edge) to 3.3 Å resolution. Native data to 4 Å from a single crystal were combined with the Ho³⁺ data set to compute isomorphous differences for phasing. The diffraction data were processed using the programs Denzo and Scalepack³⁵. SOLVE³⁶ was used to scale (using the local scale option) data from different crystals and to determine the positions of heavy atoms. The program SHARP³⁷ was used to refine them and to calculate experimental phases to the limit of the diffraction power of the Ho³⁺-containing crystals, approaching 3.1 Å (but the overall signal-to-noise ratio of the data dropped strongly after 3.3 Å resolution, owing to the anisotropic diffraction). The program DM³⁸ was used for density modification with three-fold non-crystallographic averaging. The experimental maps were very clear except for regions of the cd loop, which have high temperature factors. Model building was done using O³⁹ and Turbo⁴⁰.

Refinement was done with CNS⁴¹ using the MLHL target function, with restraints for non-crystallographic symmetry (except for the fusion loop region, where the experimental density showed clear deviation from the three-fold molecular symmetry).

In the final model, the cd loop shows considerable plasticity, adapts to the specific contact in the crystal and displays high temperature factors, reflecting high mobility and/or static disorder. The packing in the crystal explains the very high radiation sensitivity of the crystals. The crystal packing involves four different contacts, two of which, contacts 1 and 2, are made by the fusion loops and are discussed in Supplementary Information. Contact 1 is mediated by a crystallographic dyad and involves fusion loop residues 85–92 of one trimer and 93–96 in the adjacent trimer. Contact 2 relates residues in the bc loop (63–69) to residues 89–92 in the cd loop of the neighbouring trimer. Contact 3 takes place about another crystallographic dyad, relating two short β -strands, which form a short antiparallel β -sheet, between main-chain residues 139–143 at the amino terminus of strand F₀, including an N-linked glycosylation site at position 141. The carbohydrates attached to N141 also participate in this contact, resulting in interpretable electron density corresponding to seven sugar residues, including 2 N-acetyl glucosamines, a fucose and four mannose residues. Contact 4 involves the C₀D₀ loop (which is at the opposite end of the molecule from the cd loop; see Fig. 2) interacting with the FG loop of domain III. The phasing and crystallographic refinement statistics are provided in Table 1.

Fitting the atomic model to the EM reconstruction

The parameters and symmetry of the 2D hexagonal lattice ($a = 98 \text{ \AA}$, space group $p6$, implying six-, three- and two-fold axes normal to the plane of the lattice) constrain the fit such that the only degrees of freedom are a rotation about the three-fold molecular axis (which coincides with three-fold lattice axis) and a translation along it. As the trimers lie on a plane, this translation does not affect the lateral contacts between them. The pronounced triangular, propeller-like outline of the molecule results in a unique orientation about the three-fold axes in which the trimers can interact without clashing with each other. Figure 3 shows that this orientation fits relatively well the volume of the reconstruction. Because of radiation damage on the small 2D crystals due to the high electron dose used for the EM procedure, which affected the reconstructed volume, no attempt was made to optimize the fit of the model other than by visual inspection, guided by the absence of clashes with the constraints indicated above. The contacts involve residues in loops BC and C'D of domain III.

Illustrations

All the figures presented, including those in Supplementary Information, were prepared using the program RIBBONS⁴².

Received 25 August; accepted 14 November 2003; doi:10.1038/nature02239.

1. Jahn, R., Lang, T. & Sudhof, T. C. Membrane fusion. *Cell* **112**, 519–533 (2003).
2. Skehel, J. J. & Wiley, D. C. Receptor binding and membrane fusion in virus entry: the influenza hemagglutinin. *Annu. Rev. Biochem.* **69**, 531–569 (2000).
3. Weissenhorn, W. et al. Structural basis for membrane fusion by enveloped viruses. *Mol. Membr. Biol.* **16**, 3–9 (1999).
4. Danieli, T., Pelletier, S. L., Henis, Y. I. & White, J. M. Membrane fusion mediated by the influenza virus hemagglutinin requires the concerted action of at least three hemagglutinin trimers. *J. Cell Biol.* **133**, 559–569 (1996).
5. Blumenthal, R., Sarkar, D. P., Durell, S., Howard, D. E. & Morris, S. J. Dilation of the influenza hemagglutinin fusion pore revealed by the kinetics of individual cell–cell fusion events. *J. Cell Biol.* **135**, 63–71 (1996).
6. Markovic, I., Leikina, E., Zhukovsky, M., Zimmerberg, J. & Chernomordik, L. V. Synchronized activation and refolding of influenza hemagglutinin in multimeric fusion machines. *J. Cell Biol.* **155**, 833–844 (2001).
7. Zimmerberg, J. & Chernomordik, L. V. Membrane fusion. *Adv. Drug Deliv. Rev.* **38**, 197–205 (1999).
8. Blumenthal, R., Clague, M. J., Durell, S. R. & Epand, R. M. Membrane fusion. *Chem. Rev.* **103**, 53–69 (2003).
9. Helenius, A., Kartenbeck, J., Simons, K. & Fries, E. On the entry of Semliki Forest virus into BHK-21 cells. *J. Cell Biol.* **84**, 404–420 (1980).
10. Schlesinger, S. & Schlesinger, M. J. in *Fields Virology* (eds Knipe, D. M. & Howley, P. M.) 895–916 (Lippincott Williams and Wilkins, Philadelphia, 2001).
11. Lescar, J. et al. The fusion glycoprotein shell of Semliki Forest virus: an icosahedral assembly primed for fusogenic activation at endosomal pH. *Cell* **105**, 137–148 (2001).
12. Zhang, W. et al. Placement of the structural proteins in Sindbis virus. *J. Virol.* **76**, 11645–11658 (2002).
13. Rey, F. A., Heinz, F. X., Mandl, C., Kunz, C. & Harrison, S. C. The envelope glycoprotein from tick-borne encephalitis virus at 2 Å resolution. *Nature* **375**, 291–298 (1995).
14. Modis, Y., Ogata, S., Clements, D. & Harrison, S. C. A ligand-binding pocket in the dengue virus envelope glycoprotein. *Proc. Natl Acad. Sci. USA* **100**, 6899–6901 (2003).
15. Wahlberg, J. M. & Garoff, H. Membrane fusion process of Semliki Forest virus I. Low pH-induced rearrangement in spike protein quaternary structure precedes virus penetration into cells. *J. Cell Biol.* **116**, 339–348 (1992).
16. Kielian, M., Chatterjee, P. K., Gibbons, D. L. & Lu, Y. E. in *Subcellular Biochemistry* Vol. 34 *Fusion of Biological Membranes and Related Problems* (eds Hilderson, H. & Fuller, S.) 409–455 (Plenum, New York, 2000).
17. Klimjack, M. R., Jeffrey, S. & Kielian, M. Membrane and protein interactions of a soluble form of the Semliki Forest virus fusion protein. *J. Virol.* **68**, 6940–6946 (1994).
18. Gibbons, D. L. & Kielian, M. Molecular dissection of the Semliki Forest virus homotrimer reveals two functionally distinct regions of the fusion protein. *J. Virol.* **76**, 1194–1205 (2002).

19. Ahn, A., Gibbons, D. L. & Kielian, M. The fusion peptide of Semliki Forest virus associates with sterol-rich membrane domains. *J. Virol.* **76**, 3267–3275 (2002).
20. Gibbons, D. L. et al. Visualization of the target-membrane-inserted fusion protein of Semliki Forest virus by combined electron microscopy and crystallography. *Cell* **114**, 573–583 (2003).
21. Eckert, D. M. & Kim, P. S. Mechanisms of viral membrane fusion and its inhibition. *Annu. Rev. Biochem.* **70**, 777–810 (2001).
22. Wahlberg, J. M., Bron, R., Wilschut, J. & Garoff, H. Membrane fusion of Semliki Forest virus involves homotrimers of the fusion protein. *J. Virol.* **66**, 7309–7318 (1992).
23. Markosyan, R. M., Cohen, F. S. & Melikyan, G. B. HIV-1 envelope proteins complete their folding into six-helix bundles immediately after fusion pore formation. *Mol. Biol. Cell* **14**, 926–938 (2003).
24. Kemble, G. W., Danieli, T. & White, J. M. Lipid-anchored influenza hemagglutinin promotes hemifusion, not complete fusion. *Cell* **76**, 383–391 (1994).
25. Armstrong, R. T., Kushnir, A. S. & White, J. M. The transmembrane domain of influenza hemagglutinin exhibits a stringent length requirement to support the hemifusion to fusion transition. *J. Cell Biol.* **151**, 425–437 (2000).
26. Bagai, S. & Lamb, R. A. Truncation of the COOH-terminal region of the paramyxovirus SV5 fusion protein leads to hemifusion but not complete fusion. *J. Cell Biol.* **135**, 73–84 (1996).
27. Januszewski, M. M., Cannon, P. M., Chen, D., Rozenberg, Y. & Anderson, W. F. Functional analysis of the cytoplasmic tail of Moloney murine leukemia virus envelope protein. *J. Virol.* **71**, 3613–3619 (1997).
28. Melikyan, G. B., Markosyan, R. M., Brener, S. A., Rozenberg, Y. & Cohen, F. S. Role of the cytoplasmic tail of ectopic moloney murine leukemia virus Env protein in fusion pore formation. *J. Virol.* **74**, 447–455 (2000).
29. Chernomordik, L., Frolov, V. A., Leikina, E., Bronk, P. & Zimmerberg, J. The pathway of membrane fusion catalyzed by influenza hemagglutinin: restriction of lipids, hemifusion, and lipidic fusion pore formation. *J. Cell Biol.* **140**, 1369–1382 (1998).
30. Gaudin, Y. Rabies virus-induced membrane fusion pathway. *J. Cell Biol.* **150**, 601–612 (2000).
31. Markosyan, R. M., Melikyan, G. B. & Cohen, F. S. Evolution of intermediates of influenza virus hemagglutinin-mediated fusion revealed by kinetic measurements of pore formation. *Biophys. J.* **80**, 812–821 (2001).
32. Modis, Y., Ogata, S., Clements, D. & Harrison, S. C. Structure of the dengue virus envelope protein after membrane fusion. *Nature* **427**, 313–319 (2004).
33. Bressanelli, S. et al. Structure of a flavivirus envelope glycoprotein in its low-pH-induced membrane fusion conformation. *EMBO J.* (in the press).
34. Gibbons, D. L. et al. Purification and crystallization reveal two types of interactions of the fusion protein homotrimer of Semliki Forest virus. *J. Virol.* (in the press).
35. Otwinowski, Z. & Minor, W. in *Macromolecular Crystallography Part A* (eds Carter, C. W. & Sweet, R. M.) 307–326 (Academic Press, London, 1997).
36. Terwilliger, T. C. & Berendzen, J. Automated MAD and MIR structure solution. *Acta Crystallogr. D* **55**, 849–861 (1999).
37. de la Fortelle, E. & Bricogne, G. Maximum-likelihood heavy-atom parameter refinement for multiple isomorphous replacement and multiwavelength anomalous diffraction methods. *Methods Enzymol.* **276**, 472–493 (1997).
38. Cowtan, K. dm: an automated procedure for phase improvement by density modification. *Joint CCP4 ESF-EACBM Newsletter. Protein Crystallogr.* **31**, 34–38 (1994).
39. Jones, T. A. & Kjeldgaard, M. in *Macromolecular Crystallography Part B* (eds Carter, C. W. & Sweet, R. M.) 173–208 (Academic Press, London, 1997).
40. Roussel, A. & Cambillaud, C. *Silicon Graphics Geometry Partners Directory* (Silicon Graphics, Mountain View, California, 1991).
41. Brünger, A. T. et al. Crystallography & NMR system: a new software suite for macromolecular structure determination. *Acta Crystallogr. D* **54**, 905–921 (1998).
42. Carson, M. Ribbon models of macromolecules. *J. Mol. Graph.* **5**, 103–106 (1987).

Supplementary Information accompanies the paper on www.nature.com/nature.

Acknowledgements We thank S. Bressanelli, S. Duquerry and P. Fernandez Varela for their help at different stages of this work; A. Ahn and A. Urian for help with virus and protein preparation; C. Schulze-Briese and T. Tomikazi for help during diffraction data collection; Y. Gaudin for critically reading the manuscript; and J. Navaza for helpful discussions. More than 80% of the data used to determine the crystal structure were collected at synchrotron beam line X06SA of the Swiss Light Source, Paul Scherrer Institut, Villigen, Switzerland. Other synchrotron sources used were beam lines ID14 and ID29 at the European Synchrotron Radiation Facility, Grenoble, France, and beam line BW7A at DESY, Hamburg, Germany. M.K. acknowledges support from the Public Health Service and from a Cancer Center Core Support Grant from the National Cancer Institute. F.A.R. acknowledges support from the CNRS and INRA, the SESAME Program of the Région Ile-de-France, the French Fondation pour la Recherche Médicale, the Association pour la Recherche contre le Cancer, the CNRS programs “Physique et Chimie du Vivant” and “Dynamique et réactivité des assemblages biologiques”, and the European Union ENhCV consortium. D.L.G. was supported by the Medical Scientist Training Program of the Albert Einstein College of Medicine, the Albert Cass Traveling Fellowship and the CNRS.

Authors' contributions The crystallographic analyses reported in this paper were performed by F.A.R. and M.C.V.

Competing interests statement The authors declare that they have no competing financial interests.

Correspondence and requests for materials should be addressed to F.A.R. (rey@vms.cnrs-gif.fr) or M.K. (kielian@acem.yu.edu). The atomic coordinates of the EI* trimer, as well as the observed structure factors, have been deposited in the Protein Data Bank under accession code 1RER.